

Tidal and general relativistic effects in rocky planet formation at the sub-stellar mass limit using N-body simulations

Mariana B. Sánchez^{1,2*}, Gonzalo C. de Elía^{1,2}, and Juan José Downes³

¹ Facultad de Ciencias Astronómicas y Geofísicas, Universidad Nacional de La Plata, Paseo del Bosque S/N (1900), La Plata, Argentina.

² Instituto de Astrofísica de La Plata, CCT La Plata-CONICET-UNLP, Paseo del Bosque S/N (1900), La Plata, Argentina.

³ Centro Universitario Regional del Este, Universidad de la República, AP 264, Rocha 27000, Uruguay.

ABSTRACT

Context. Recent observational results show that very low mass stars and brown dwarfs are able to host close-in rocky planets. Low-mass stars are the most abundant stars in the Galaxy and the formation efficiency of their planetary systems is relevant in the computation of a global probability of finding Earth-like planets inside habitable zones. Tidal forces and relativistic effects are relevant in the latest dynamical evolution of planets around low-mass stars and their effect on the planetary formation efficiency still needs to be addressed.

Aims. Our goal is to evaluate the impact of tidal forces and relativistic effects on the formation of rocky planets around a star close to the sub-stellar mass limit, in terms of the resulting planetary architectures and its distribution according to the corresponding evolving habitable zone.

Methods. We performed a set of N -body simulations spanning the first 100 Myr of the evolution of two systems composed respectively by 224 embryos with a total mass $0.25M_{\oplus}$ and 74 embryos with a total mass $3M_{\oplus}$ around a central object of $0.08M_{\odot}$. For both scenarios, we compared the planetary architectures that result from simulations that are purely gravitational with those from simulations that include the early contraction and spin up of the central object, the distortions and dissipation tidal terms and general relativistic effects.

Results. We found that the inclusion of these effects allow the formation and survival of a close-in ($r < 0.07$ au) population of rocky planets with masses in the range $0.001 < m/M_{\oplus} < 0.02$ in all the simulations of the less massive scenario, and a close-in population with masses $m \sim 0.35M_{\oplus}$ in just few of the simulations of the more massive scenario. The surviving close-in bodies suffered high number of collisions along the integration time of the simulations which play an important role in their final masses. However, all of them conserved their initial amount of water in mass along the integration time.

Conclusions. The incorporation of tidal and general relativistic effects allow the formation of an in-situ close-in population located in the habitable zone of the system. Thus, both effects are relevant during the formation of rocky planet and their early evolution around stars close to the sub-stellar mass limit, in particular when low-mass planetary embryos are involved.

Key words. planets and satellites: formation - planets and satellites: terrestrial planets - stars: low-mass - planet-star interactions - methods: numerical

1. Introduction

During the last decades several observational and theoretical results suggest the formation of rocky planets is a common process around stars of different masses (e.g. Cumming et al. 2008; Mordasini et al. 2009; Howard 2013; Ronco et al. 2017). Particularly, observations and modeling have proven the existence and formation of rocky planets around very low mass stars (VLMS) and brown dwarfs (BDs) (e.g. Payne & Lodato 2007; Raymond et al. 2007; Gillon et al. 2017). These achievements are relevant because VLMS are the most abundant stars in the Galaxy and together with BDs are within the closest solar neighbors (e.g. Padoan & Nordlund 2004; Henry 2004; Bastian et al. 2010). Thus it allows for surveys of rocky planets even in habitable zones, around numerous stellar samples and through different observational techniques. This could be a crucial observa-

tional test of the processes driving the planet formation as suggested by theoretical modeling.

Although the detection of rocky planets around BDs is still challenging some systems have been discovered (e.g. Kubas et al. 2012; Gillon et al. 2017; Grimm et al. 2018; Zechmeister et al. 2019). By using photometry from *Spitzer*, He et al. (2017) reported an occurrence rate $\sim 87\%$ of planets with radius $0.75 < R/R_{\oplus} < 1.25$ and orbital periods $1.7 < P/\text{days} < 1000$ around a sample of 44 BDs. From the M-type low mass stars monitored by *Kepler* mission, Mulders et al. (2015) found that planets around VLMS are located close to their hosts stars having an occurrence rate of small planets ($1 < R/R_{\oplus} < 3$) which is 3 to 4 times higher than for Sun-like stars, while Hardegree-Ullman et al. (2019) estimated a mean number of 1.19 planets per mid-type M dwarfs with radius $0.5 < R/R_{\oplus} < 2.5$ and orbital periods $0.5 < P/\text{days} < 10$. The current *SPHERE* imager together with *ESPRESSO* spectrograph are already detecting Earth-sized planets around G, K

* e-mail:msanchez@fcaglp.unlp.edu.ar

and M dwarfs (Lovis et al. 2017; Hojjatpanah et al. 2019) and *CARMENES* spectrograph is searching for exoplanets around M dwarfs and already found two Earth-mass planets around a M7 BD (Zechmeister et al. 2019). It is expected that the ongoing and upcoming transit searches such as *TESS* (Barclay et al. 2018) and *PLATO* (Ragazzoni et al. 2016) will find most of the nearest transiting systems in the next years opening the new era of atmospheric characterization of terrestrial-sized 0.5° for the initial inclinations. The regarding orbital elements, argument of periastron ω , longitude of the ascending node Ω and mean anomaly

Current observations suggest that does not seem to be a discontinuity in the general properties of the circumstellar discs around VLMS and BDs (e.g. Luhman 2012). In particular, the dust growth to millimeter and centimeters sizes on the disk mid plane of BDs is similar than in VLMS disks, as has been inferred for few BDs observed with ALMA and CARMA (Ricci et al. 2012, 2013, 2014), which suggests that also similar processes in the evolution of disk could take place at both sides of the sub-stellar mass limit.

Payne & Lodato (2007) investigated planet formation around low-mass objects using a standard core accretion model. They found that the formation of Earth-like planets is possible even around BDs, and that planets with masses up to $5 M_\oplus$ can be formed. They remarked the mass-distribution of the resulting planets is strongly correlated with the disk masses. In particular, if the BD has a disk mass of the order of a few Jupiter masses then only 10% of BDs might host planets with masses bigger than $0.3 M_\oplus$. Through dynamical simulations of terrestrial planet formation from planetary embryos, Raymond et al. (2007) found that the masses of planets located inside the habitable zone decrease while decreasing the mass of the host star, finding small and dry planets around low-mass stars. Using *N*-body simulations with diverse water-mass fractions for objects beyond the snowline, Ciesla et al. (2015) found both dry and water-rich planets close to low-mass stars. By studying planet formation around different host stars, their simulations predict that a greater number of compact and low-mass planets are located around low-mass stars while higher-mass stars will be hosting fewer and more massive planets. Recently, Coleman et al. (2019) while studying planet formation around low-mass stars similar to Trappist-1, considering different accretion scenarios, found water-rich rocky planets with periods $0.5 < P/\text{days} < 1000$. Furthermore, Miguel et al. (2019) studied planet formation around BDs and low-mass stars by using a population synthesis code and found planets with a wide ice to rock ratio.

The treatment regarding the formation and evolution of rocky planetary systems around low mass objects is still under study. Planets around these objects are thought to form close to them in a region where tides are very strong and lead to significant orbital changes (Papaloizou & Terquem 2010; Barnes et al. 2010; Heller et al. 2010). The fact that in their first hundred Myr BDs as well as VLMS are collapsing and spinning up with time allows the close-in tidal-locked bodies population around them to experience many different dynamical evolutions (Bolmont et al. 2011). In their works, Bolmont et al. (2013, 2015) showed the importance of incorporating tidal effects and general relativity as well as the effect of rotation-induced flaring in the dynamical and tidal evolution of multi-planetary systems, particularly those having close-in bodies.

In this work we present the incorporation of these effects in a set of *N*-body simulations to study rocky planet formation from a sample of embryos around an object with a mass of $0.08 M_\odot$ close to the sub-stellar mass limit, in a spanning

period of 100 Myr in order to improve predictions on planetary system architectures. We focus on the evaluation of how relevant are tidal and relativistic effects during rocky planet formation around an object at the sub-stellar mass limit. Our aim is to estimate dynamical properties of the resulting close-in bodies population and the efficiency of forming planets that remind in the habitable zone of the system.

In Section 2 we briefly describe the early gravitational collapse and rotation rates of VLMS and BDs. In Section 3 we show the modeling of the habitable zone around a star close to the sub-stellar mass limit. In Section 4 we describe the considered protoplanetary disk model based on observations. In Section 5 we explain the numerical method used to include tidal forces and general relativity effects into the *N*-body simulations. In Section 6 we describe the resulting planetary systems and, finally in Section 7 we summarize the conclusions and future works.

2. Collapse and rotation of young VLMS and BD

The BDs are stellar structures unable to reach the necessary core temperatures and densities to sustain stable hydrogen fusion. For solar metallicity, the sub-stellar mass limit which separates BDs from VLMS is $0.072 M_\odot$ (Baraffe et al. 2015). During the first ~ 100 Myr of their evolution BDs and VLMS share several properties such as the presence of circumstellar disks at different evolutionary stages (e.g. Luhman 2012), the formation of planets around them, their gravitational collapse and the subsequent increase of their rotation rates with time. These last two properties are particularly relevant in our modeling.

In the case of VLMS, the collapse stops when they reach the main sequence at ages around ~ 100 Myr while BDs keep collapsing slowly towards a degenerate structure unable to sustain stable hydrogen fusion (e.g. Kumar 1963; Hayashi & Nakano 1963).

Available observations show that BDs have mean rotational periods shorter than those from VLMS which have been interpreted as a indication of a low efficiency of the magnetic braking on the early spin up in the sub-stellar mass domain (Mohanty et al. 2002; Scholz et al. 2015). The spin rate of the the main object sets the position of the co-rotation radius r_{corot} which is the mid-plane orbital distance where the mean orbital velocity n of a planet is equal to the rotational velocity Ω_\star of the central object. In the case of a VLMS and BD, r_{corot} shrinks while the object spins up. This behavior is essential for the treatment of close-in bodies because their orbital evolution depends on the initial eccentricity e and semi-major axis a with respect to the location of r_{corot} .

3. Modeling the Habitable zone

The classical habitable zone (CHZ) is the circular region around a single star or a multiple star system where a rocky planet can retain liquid water in its surface (Kasting et al. 1993). The CHZ definition assumes that the most important greenhouse gases for habitable planets orbiting main-sequence stars are CO_2 and H_2O . This assumption is an extension towards potentially habitable exoplanets of the idea that the long-term (~ 1 Myr) carbonate-silicate cycle on Earth acts as a planetary thermostat that regulates the surface temperature (Watson et al. 1981; Walker et al. 1981; Kasting 1988).

For study potentially habitable exoplanets around a non solar-type star it is necessary to take into account the relation between the albedo and the effective temperature of the central

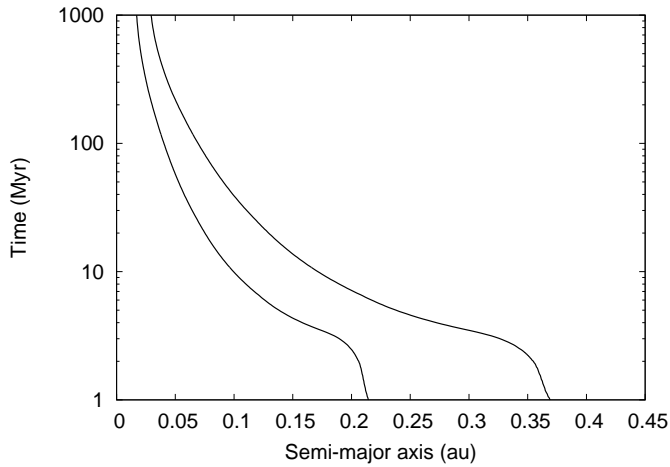


Fig. 1. Evolution of the habitable zone around a star of $0.08 M_{\odot}$ in a period of 1 Gyr.

star. By extrapolating the cases studied by Kasting et al. (1993), the inner and outer limits of the isolated habitable zone (IHZ) for stars with effective temperatures in between $3700 < T_{\text{eff}}/\text{K} < 7200$ can be calculated as in Selsis et al. (2007) by

$$l_{\text{int}} = (l_{\text{in},\odot} - a_{\text{in}}T_{\star} - b_{\text{in}}T_{\star}^2) \left(\frac{L_{\star}}{L_{\odot}} \right)^{\frac{1}{2}}, \quad (1)$$

$$l_{\text{out}} = (l_{\text{out},\odot} - a_{\text{out}}T_{\star} - b_{\text{out}}T_{\star}^2) \left(\frac{L_{\star}}{L_{\odot}} \right)^{\frac{1}{2}}, \quad (2)$$

where $l_{\text{in},\odot} = 0.97$ au and $l_{\text{out},\odot} = 1.67$ au are the inner and outer limits of a system with a Sun-like star as central object, considering runaway greenhouse and maximum greenhouse values respectively (Kopparapu et al. 2013b,a), and $a_{\text{in}} = 2.7619 \times 10^{-5} \text{ auK}^{-1}$, $b_{\text{in}} = 3.8095 \times 10^{-9} \text{ auK}^{-2}$, $a_{\text{out}} = 1.3786 \times 10^{-4} \text{ auK}^{-1}$ and $b_{\text{out}} = 1.4286 \times 10^{-9} \text{ auK}^{-2}$ are empirically determined constants; L_{\odot} and L_{\star} are the luminosity of the Sun and the considered star, and the temperature of the star is $T_{\star} = T_{\text{eff}} - 5700\text{K}$ where T_{eff} can be expressed by

$$T_{\text{eff}} = \left(\frac{L_{\star}}{4\pi\sigma R_{\star}^2} \right)^{\frac{1}{4}}, \quad (3)$$

with R_{\star} the radius of the central object and σ is the Stefan-Boltzmann constant. As in Barnes et al. (2013) who studied habitable planets around BDs, we extended the calculation of the IHZ to the sub-stellar mass limit. Thus, in this work l_{in} and l_{out} represent, respectively, the inner and outer limits of the IHZ around a $0.08 M_{\odot}$ object. We used R_{\star} , L_{\star} and T_{eff} as a function of time as predicted by the models from Baraffe et al. (2015)¹. In Fig. 1 we show the evolution of the IHZ of an object of $0.08 M_{\odot}$. While the object is evolving, L_{\star} , R_{\star} and T_{eff} decrease with time and the location of the IHZ become narrower and closer to the sub-stellar object. When the central object is 1 Myr-old, $l_{\text{in}} = 0.214$ au and $l_{\text{out}} = 0.369$ au while at 1 Gyr-old, $l_{\text{in}} = 0.017$ au and $l_{\text{out}} = 0.029$ au. It is worth noting that the IHZ is located more than ten times closer to the central object after this period of time.

¹ <http://perso.ens-lyon.fr/isabelle.baraffe/BHAC15dir/>

4. Protoplanetary disk description

In this section we describe the protoplanetary disk model that we adopted for the $0.08 M_{\odot}$ central object. We calculate the dust species that could survive inside our region of study to know the available material for the formation of bigger structures such as protoplanetary embryos. We discriminate two scenarios of work motivated by the diversity of disk masses and the exoplanet mass distribution around low-mass objects observed. Finally, we compare our model with other used by different authors in the literature.

4.1. Region of study

Our region of study is defined between an inner radius $r_{\text{init}} = 0.015$ au and an outer radius of $r_{\text{final}} = 1$ au. The selection of the inner radius was made by considering that tidal effects allow a planet located at this distance to survive without colliding with the central object for certain values of its eccentricity (Bolmont et al. 2011). The outer radius was defined in a way that the habitable zone and an outer region of water-rich embryos are contained in our region of study.

We evaluated the consistency of the selection of r_{init} with the sublimation radius for different dust species by analyzing those species that could survive inside our region of study. We computed sublimation radii for a variety of species using the model of Kobayashi et al. (2011). Sublimation temperatures were estimated by Pollack et al. (1994). In Fig. 2 we showed the variation of the sublimation radii with time for different species, in contrast with the co-rotation radii r_{corot} , the inner radii r_{init} of the region and the radius of the stellar object R_{\star} . Components like iron and volatile and refractory organics could survive during the first Myr inside our region of study.

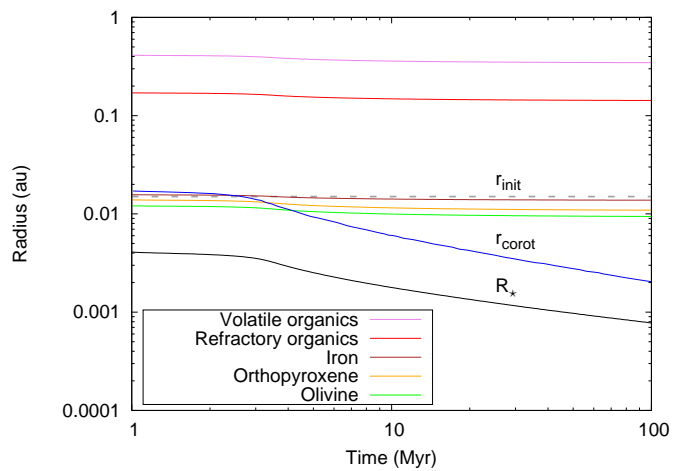


Fig. 2. Sublimation radii for different dust grain species and its comparison with the co-rotation r_{corot} , the stellar radius R_{\star} and the inner radii of our region of study r_{init} .

4.2. Protoplanetary disk model

The parameter that determines the distribution of the material in the disk is the surface density Σ . From physical models of viscous accretion disks (see Lynden-Bell & Pringle 1974;

Hartmann et al. 1998), we adopted the dust surface density profile given by

$$\Sigma_s(r) = \Sigma_{0s} \eta_{\text{ice}} \left(\frac{r}{r_c} \right)^{-\gamma} e^{-(r/r_c)^{2-\gamma}}. \quad (4)$$

This profile is routinely used for the interpretation of observational results in a wide range of stellar masses down to the substellar mass regime (e.g. Andrews et al. 2009; Andrews et al. 2010; Guilloteau et al. 2011; Testi et al. 2016). The value r represents the radial coordinate in the mid-plane of the disk, r_c is the characteristic radius of the disk, γ is the factor which determines the density gradient and η_{ice} represents the increase in the amount of solid material due to the condensation of water beyond the snowline $r = r_{\text{ice}}$. For large samples of stars Andrews et al. (2009, 2010) found that the factor γ can take values between 1.1, having a mean value of 0.9. On the other hand, using a different technique Isella et al. (2009) found values for γ between -0.8 and 0.8, with a mean value of 0.1. For BD and VLMS, the lower and upper bounds for γ are -1.4 and 1.4 respectively, having a mean value close to 1 (Testi et al. 2016). We took $r_c = 15$ au and $\gamma = 1$ which are consistent with the latest observations of disks around BDs and VLMS (Ricci et al. 2012, 2013, 2014; Testi et al. 2016; Hendler et al. 2017). We fixed the location of the snowline at $r_{\text{ice}} = 0.42$ au (see Appendix A). Following the works of Lodders (2003); Lodders et al. (2009), we proposed that inside the snowline $\eta_{\text{ice}} = 1$ and beyond the snowline $\eta_{\text{ice}} = 2$. This jump of a factor 2 in the solid surface density profile is related with the water gradient distribution. Thus, we considered that bodies beyond r_{ice} present 50% of water in mass while bodies inside r_{ice} have just 0.01% water in mass. This small percentage of water for bodies inside the snowline is given considering that the inner region was affected by water-rich embryos from beyond the snowline during the gaseous phase related with the evolution of the disk. The water distribution is assigned to each body at the beginning of our simulations. We remark that the highest initial percentage of water in mass is going to fix the value of the maximum percentage of water in mass that a resulting planet could have given the fact that the N -body code treats the collisions as perfectly inelastic ones, so bodies conserve their mass and water amount of water in mass in each collision.

By assuming an axial symmetric distribution for the solid material, we can express the dust mass of the disk M_{dust} by

$$M_{\text{dust}} = \int_0^{\infty} 2\pi r \Sigma_s(r) dr. \quad (5)$$

Note that solving Eq. (5) means solve two integral due to the jump in the content of water in the disk given by η_{ice} at r_{ice} . Thus we can estimate the normalization constant for the solid component of the disk Σ_{0s} for a given value of the solid mass in the disk.

4.3. Twofold parameterization of disk density

As discussed by Manara et al. (2018) there is a robust observational evidence about protoplanetary disks being less massive than the known exoplanet populations. The authors suggested two mechanisms for such discrepancy in mass: an early formation of planetary cores at ages $< 0.1 - 1$ Myr when disks may be more massive, and disks are replenished by fresh material from the environment during their lifetimes. In order to consider the current uncertainties in the estimations of disk masses, we made

the disk parameterization of the surface density profile from Eq. (4) for two distinct values of M_{dust} . We refer both cases as the following *mass scenarios*:

- **The disk scenario (S1):** is based on the latest observational results on the masses of dust in protoplanetary disks. We assumed a $M_{\text{dust}} = 9 \times 10^{-6} M_{\odot}$ ($\sim 3 M_{\oplus}$) from the average of dust masses obtained from the observations of BDs and VLMS made with ALMA (see references in Section 4.2). If we assumed a gas to dust ratio of 100:1 then is equivalent to take a $M_{\text{disk}} = 1.1\% M_{\star}$.
- **The planetary systems scenario (S2):** is based on the observational results on the masses of exo-planetary systems. We assumed $M_{\text{dust}} = 9 \times 10^{-5} M_{\odot}$ ($\sim 30 M_{\oplus}$) regarding the currently terrestrial exoplanets detection around BDs (e.g. Kubas et al. 2012; Gillon et al. 2017; Grimm et al. 2018). If we assumed a gas to dust ratio of 100:1 then is equivalent to take a $M_{\text{disk}} = 11\% M_{\star}$. In this case, we increased the percentage of mass in order to extend the available solid material in the disk in our region of study to form rocky planets.

4.4. Contrasting Σ parameterization

Many authors also propose a power-law surface density profile to model protoplanetary disks (e.g. Ciesla et al. 2015; Testi et al. 2016). Thus why we compared the model proposed in this work (Eq. 4) with a power-law density profile:

$$\Sigma_{\text{sp}}(r) = \Sigma_{\text{sp}0} \eta_{\text{ice}} \left(\frac{r}{r_0} \right)^{-p} \quad (6)$$

with r_0 and p are equivalent to r_c and γ in the exponentially tapered density profile. In Fig. 3 we show the comparison of both density profiles considering the same initial parameters that we choose to describe $\Sigma_s(r)$ (see Section 4.2). As an example, we selected three different disk masses M_{disk} : 0.1%, 1% and 10% of the mass of the central object and assumed a gas to dust ratio of 100 : 1. We see that the power-law profiles do not show significant differences with the exponentially tapered density profiles within our region of study.

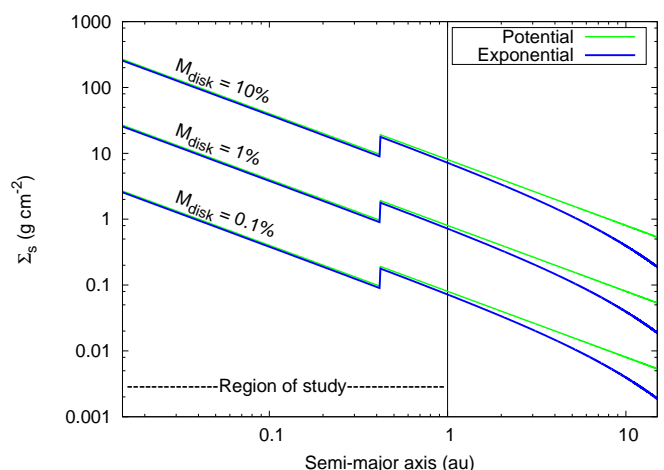


Fig. 3. Power law (green line) and exponential tapered (blue line) surface density profiles along the protoplanetary-planetary disk for disk total mass M_{disk} of 0.1%, 1% and 10% of the mass of the central object of $0.08 M_{\odot}$. The region of study ($0.015 < r/\text{au} < 1$) is indicated.

5. Numerical model

In this section we describe the treatment of planet formation around an object of $0.08 M_{\odot}$ by including a protoplanetary embryo distribution interacting with the main object. We developed a set of N -body simulations with the well known MERCURY code (Chambers 1999) by incorporating tidal and general relativistic acceleration corrections as external forces. Thus the dynamical evolution of protoplanetary embryos was affected not only by gravitational interactions between them and with the star, but also by tidal distortions and dissipation, as well as general relativistic effects. The stellar contraction and rotational period evolution was included in the code as well as a fixed pseudo-synchronization period for protoplanetary embryos along the 100 Myr integration time of our simulations.

5.1. Tidal model

In this work we followed the equilibrium tide model (Hut 1981; Eggleton et al. 1998), that was re-derived by Bolmont et al. (2011), which considers both the tide raised by the BD on the planet and by the planet on the BD in the orbital evolution of planetary systems and takes into account the spin up and the contraction of the BD. They followed the constant time-lag model and assumed constant internal dissipation for the BD and the planets involved.

5.1.1. Tidal distortion and dissipation terms

Following the equilibrium tidal model, we incorporated both, tidal distortions and dissipation terms, considering the tide raised by the star on each protoplanetary embryo and by each protoplanetary embryo on the star and neglected the tide between embryos.

Tidal interactions will produce deformations on the bodies that will lead, considering a heliocentric reference frame, to precession of the argument of periastron ω and a semi-major axis a and eccentricity e decay, which can be interpreted respectively as distortions and dissipation terms.

The correction in the acceleration of each protoplanetary embryo produced by the tidal distortion term was taken from Hut (1981) (for an explicit expression see Beaugé & Nesvorný (2012)) and is given by

$$\mathbf{f}_{\omega} = -3 \frac{\mu}{r^8} \left[k_{2,*} \left(\frac{M_p}{M_*} \right) R_*^5 + k_{2,p} \left(\frac{M_*}{M_p} \right) R_p^5 \right] \mathbf{r}, \quad (7)$$

where \mathbf{r} is the position vector of the embryo with respect to the central object, $k_{2,*} = 0.307$ and $k_{2,p} = 0.305$ are the potential Love numbers of degree 2 of the star and the embryo respectively (Bolmont et al. 2015), $\mu = G(M_* + M_p)$, G is the gravitational constant and M_* , R_* , M_p and R_p are, respectively, the masses and radius of the star and the protoplanetary embryo under the approximation that these objects can instantaneously adjust their equilibrium shapes to the tidal force and considering only up to the second-order harmonic distortions (Darwin 1908).

The evolution of R_* was taken from the models of Baraffe et al. (2015) while the value of R_p of each protoplanetary embryo was calculated by considering each of them as a spherical body with a fixed volume density $\rho = 5 \text{ gr/cm}^3$.

The timescale associated with the tidal dissipation term was calculated based on the work of Sterne (1939) by considering both the star tide and the embryo tide, and it is given by

$$t_{\text{tide}} \sim \frac{2\pi a^5}{7.5nf(e)} \left(\frac{M_* M_p}{k_{2,*} M_p^2 R_*^5 + k_{2,p} M_*^2 R_p^5} \right), \quad (8)$$

with $f(e) = (1 - e^2)^{-5} [1 + (3/2)e^2 + (1/8)e^4]$.

The acceleration correction of each protoplanetary embryo induced by the tidal dissipation term, which produces a and e decay, was obtained from Eggleton et al. (1998) which, after doing some algebra, equals the following expression from Beaugé & Nesvorný (2012)

$$\mathbf{f}_{\text{ac}} = -3 \frac{\mu}{r^{10}} \left[\frac{M_p}{M_*} k_{2,*} \Delta t_* R_*^5 (2\mathbf{r}(\mathbf{r} \cdot \mathbf{v}) + r^2(\mathbf{r} \times \boldsymbol{\Omega}_* + \mathbf{v})) \right] - 3 \frac{\mu}{r^{10}} \left[\frac{M_*}{M_p} k_{2,p} \Delta t_p R_p^5 (2\mathbf{r}(\mathbf{r} \cdot \mathbf{v}) + r^2(\mathbf{r} \times \boldsymbol{\Omega}_p + \mathbf{v})) \right], \quad (9)$$

where \mathbf{v} is the velocity vector of the embryo, Δt_* and Δt_p are the time-lag model constants for the star and the protoplanetary embryo respectively. The factors $k_{2,*} \Delta t_*$ and $k_{2,p} \Delta t_p$ are related with the dissipation factors by

$$k_{2,p} \Delta t_p = \frac{3R_p^5 \sigma_p}{2G} \quad k_{2,*} \Delta t_* = \frac{3R_*^5 \sigma_*}{2G} \quad (10)$$

with the dissipation factor for each protoplanetary embryo $\sigma_p = 8.577 \times 10^{-50} \text{ g}^{-1} \text{ cm}^{-2} \text{ s}^{-1}$, the same dissipation factor estimated for the Earth (Neron de Surgy & Laskar 1997), and the dissipation factor of the central object is $\sigma_* = 2.006 \times 10^{-60} \text{ g}^{-1} \text{ cm}^{-2} \text{ s}^{-1}$ (Hansen 2010).

In the constant time-lag model, in which the time-lag constant Δt_* is independent of the tidal frequency, the rotation of the companions leads to pseudo-synchronization (Hut 1981; Eggleton et al. 1998). In preliminary simulations, Leconte et al. (2010); Bolmont et al. (2011, 2013) verified the fact that a planet reaches the pseudo-synchronization very quickly in its evolution. For a planet being at pseudo-synchronization means that its rotation tends to be synchronized with the orbital angular velocity at periastron, where the tidal interactions are stronger (Hut 1981). As in Bolmont et al. (2011), we fixed each protoplanetary embryo at pseudo-synchronization (Hut 1981) in each time-step of our simulations as follows

$$\Omega_p = \frac{(1 + (15/2)e^2 + (45/8)e^4 + (5/16)e^6)}{(1 + 3e^2 + (3/8)e^4)(1 - e^2)^{3/2}} n, \quad (11)$$

where Ω_p is the protoplanetary embryo rotation velocity.

If $e = 0$, then the embryo is in perfect synchronization thus $\Omega_p = n$ and only the tide of the central object remain. When e is small, the tide of the main object dominates and determines the evolution of the embryo: if the embryo is located beyond r_{corot} , then $\Omega_p < \Omega_*$, $\frac{da}{dt} > 0$ so the embryo is pushed outward, and if it is inside, $\Omega_p > \Omega_*$, $\frac{da}{dt} < 0$ so the embryo is pulled inward. On the other hand, when the e is high, the embryo tide will prevail. In this case, the embryo is pulled inward. This is always true because for a body in pseudo-synchronization the body tide always acts to decrease the orbital distance (Leconte et al. 2010).

The main object rotational velocity Ω_* was calculated following the tidal model proposed by Bolmont et al. (2011) who integrated its evolution due to its contraction and the influence of orbiting planets, and calibrated their results with a set of observational determined Ω_* for VLMS and BDs at different ages from Herbst et al. (2007). Thus the evolution of Ω_* can be expressed as follow

$$\Omega_*(t) = \Omega_*(t_0) \left[\frac{r_{\text{gyr}}^2(t_0)}{r_{\text{gyr}}^2(t)} \left(\frac{R_*(t_0)}{R_*(t)} \right)^2 \times \exp \left(\int_{t_0}^t f_i dt \right) \right], \quad (12)$$

(e.g. Bolmont et al. 2011) where r_{gyr}^2 is the square of the radius of gyration defined as $r_{\text{gyr}}^2 = \frac{I_*}{M_* R_*}$ with I_* the moment of inertia of the main object (Hut 1981). The function f_i is given by

$$f_i = \frac{1}{\Omega_*} \frac{d\Omega_*}{dt}. \quad (13)$$

If we considered r_{gyr}^2 and R_* as constant values (Bolmont et al. 2011), then

$$f_i = -\frac{\gamma_*}{t_{\text{dis},*}} \left[\text{No1}(e) - \frac{\Omega_*}{n} \text{No2}(e) \right] \quad (14)$$

with $\gamma_* = \frac{h}{I_* \Omega_*}$, h the orbital angular momentum, $t_{\text{dis},*}$ the dissipation timescale of the central object (see below) and the functions $\text{No1}(e)$ and $\text{No2}(e)$ dependent on the e of the planetary companion given by

$$\text{No1}(e) = \frac{1 + (15/2)e^2 + (45/8)e^4 + (5/16)e^6}{(1 - e^2)^{13/2}} \quad (15)$$

$$\text{No2}(e) = \frac{1 + 3e^2 + (3/8)e^4}{(1 - e^2)^5}.$$

If just terrestrial planets are considered orbiting the host object, then f_i is small and the sub-stellar object rotation period is mainly determined by the conservation of angular momentum so by the initial rotation period (Bolmont et al. 2011). Thus why we numerically integrated Eq. (12) independently of the dynamics of the planetary system. We considered that the radius R_* evolves according to the structure and atmospheric models from Baraffe et al. (2015), but fixing its value for each time-step of our integration which was small enough to be considered constant in order to simplify the integration and be able to use Eq. (14). Also we assumed one Earth-like planet orbiting the main-object with random initial values for e and a , inside our region of study. From the different orbital elements initially given to the Earth-like planet, we verified that the evolution of Ω_* was mainly determined by the evolution of the sub-stellar object and similar to the one achieved by Bolmont et al. (2011). In Fig. 4 we show the resulting evolution of the rotational period and the corresponding R_* in a period from 1 Myr to 100 Myr.

The dissipation timescales for eccentric orbits are determined from the secular tidal evolution of a and e (see Hansen 2010; Bolmont et al. 2011, 2013) as t_a and t_e respectively by

$$\frac{1}{t_a} = \frac{1}{a} \frac{da}{dt} = -\frac{1}{t_{\text{dis},p}} \left[\text{Na1}(e) - \frac{\Omega_p}{n} \text{Na2}(e) \right] - \frac{1}{t_{\text{dis},*}} \left[\text{Na1}(e) - \frac{\Omega_*}{n} \text{Na2}(e) \right] \quad (16)$$

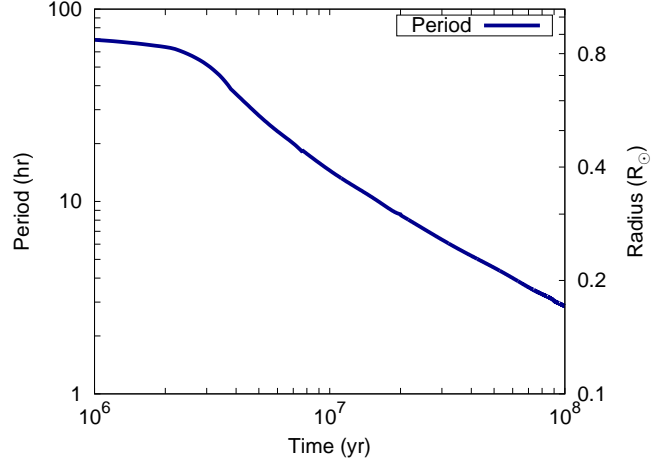


Fig. 4. Rotation period evolution of an object of $0.08 M_{\odot}$ based on Bolmont et al. (2011) associated with its radius contraction with time taken from Baraffe et al. (2015).

$$\frac{1}{t_e} = \frac{1}{e} \frac{de}{dt} = -\frac{9}{2t_{\text{dis},p}} \left[\text{Ne1}(e) - \frac{11}{18} \frac{\Omega_p}{n} \text{Ne2}(e) \right] - \frac{9}{2t_{\text{dis},*}} \left[\text{Ne1}(e) - \frac{11}{18} \frac{\Omega_*}{n} \text{Ne2}(e) \right]. \quad (17)$$

where $t_{\text{dis},p}$ and $t_{\text{dis},*}$ are the dissipation timescales for circular orbits for the embryo and the main object respectively, and Na1 , Na2 , Ne1 and Ne2 factors which take places in eccentric orbits defined by

$$\begin{aligned} t_{\text{dis},p} &= \frac{1}{9} \frac{M_p}{M_*(M_p + M_*)} \frac{a^8}{R_p^{10}} \frac{1}{\sigma_p}, \\ t_{\text{dis},*} &= \frac{1}{9} \frac{M_*}{M_p(M_p + M_*)} \frac{a^8}{R_*^{10}} \frac{1}{\sigma_*}, \\ \text{Na1}(e) &= \frac{1 + (31/2)e^2 + (255/8)e^4 + (185/16)e^6 + (25/64)e^8}{(1 - e^2)^{15/2}}, \\ \text{Na2}(e) &= \frac{1 + (15/2)e^2 + (45/8)e^4 + (5/16)e^6}{(1 - e^2)^6}, \\ \text{Ne1}(e) &= \frac{1 + (15/4)e^2 + (15/8)e^4 + (5/64)e^6}{(1 - e^2)^{13/2}}, \\ \text{Ne2}(e) &= \frac{1 + (3/2)e^2 + (1/8)e^4}{(1 - e^2)^5}. \end{aligned} \quad (18)$$

5.2. General relativistic effect

The important effect derived from the General Relativity Theory (GRT) which affect the dynamic of planetary systems is the precession of ω (Einstein 1916). In our case, we considered that

just only the main object contributes with relevant corrections. As we worked in the reference frame of the star, the associated correction in the acceleration of the embryo is

$$\mathbf{f}_{\text{GR}} = \frac{GM_{\star}}{r^3 c^2} \left[\left(\frac{4GM_{\star}}{r} - \mathbf{v}^2 \right) \mathbf{r} + 4(\mathbf{v} \cdot \mathbf{r}) \mathbf{v} \right], \quad (19)$$

with c the speed of light. The Eq. (19) was proposed by Anderson et al. (1975), who worked under the Parameterize Post Newtonian theories arriving to a relative correction associated with two parameters β and γ , which are equal to unit in the GRT case. This expression is used in several works including relativistic corrections (e.g. Quinn et al. 1991; Shahid-Saless & Yeomans 1994; Varadi et al. 2003; Benitez & Gallardo 2008; Zanardi et al. 2018). The timescale associated with the precession of the longitude of periastron is given by

$$t_{\text{GR}} \sim 2\pi \frac{a^{\frac{5}{2}} c^2 (1 - e^2)}{3G^{\frac{3}{2}} (M_{\star} + M_{\text{p}})^{\frac{3}{2}}}. \quad (20)$$

5.3. Test simulations

We made a set of N -body simulations in order to test the agreement between the external forces that we incorporated in `MERCURY` code and the timescale associated with them.

For testing the precession of ω we developed two simulations: one that included the tidal distortion term and other one that included the general relativistic (GR) correction. In Fig. 5 we show the apsidal precession timescale of a planet with $1 M_{\oplus}$ orbiting around a 1 Myr sub-stellar object of $0.08 M_{\odot}$ with initial values $a = 0.01 \text{ au}$ and $e = 0.1$ for both simulations made. Our results shows the apsidal precession of 360° is completed, respectively, in 14750 yr and 3060 yr which results to be in agreement with the time predicted by the timescales associated to each correction term in Eqs. (20) and (8). We remark that these timescale values depend on physical parameters of the protoplanetary embryos and the sub-stellar object, as well as on the initial orbital elements. For instance, if the protoplanets are smaller than the Earth in mass and radius, then the relativistic effect result more relevant than the tidal distortion regarding the precession of ω .

To test the analytic expressions for the tidal dissipation with the timescales of e and a decay we developed an N -body simulation which includes the dissipation term. Our aim was to compare our results with the ones obtained by Bolmont et al. (2011) who used the analytic tidal model. In their work, they represent, between others, the evolution of a , e and the rotation period of a planet of $1 M_{\oplus}$ evolving around a BD of $0.04 M_{\odot}$. We chose as initial values $a = 0.017242 \text{ au}$ and $e = 0.744$. The semi-major axis selected represent the a_{switch} , that is the one that determines the behavior of the protoplanet and separates inward migration and crash from inward migration but survival of the protoplanet or outward migration.

In Fig. 6 we showed the evolution of a , e and the pseudo-synchronization period P_{p} of a $1 M_{\oplus}$ planet around an evolving $0.04 M_{\odot}$ BD. In the middle panel, we also show r_{corot} evolution, while in the bottom panel we included the rotation period of the BD, P_{\star} (dashed-lines). First, as $P_{\star} > P_{\text{p}}$ the planet moves inward the central object. Under this condition, even tough $a = r_{\text{corot}}$, the orbit is not circular and the planet continue moving inward. When $P_{\star} = P_{\text{p}}$, the orbit is circular and

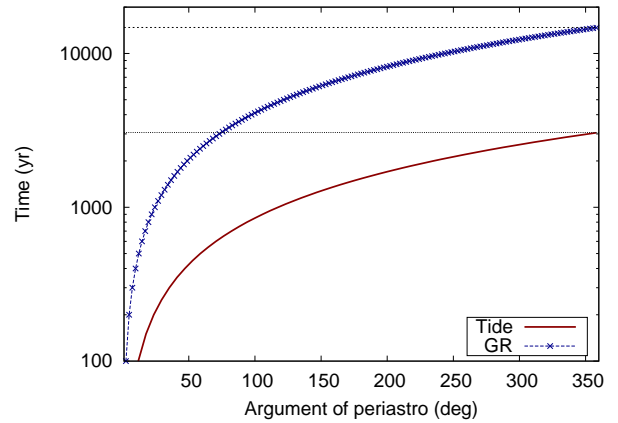


Fig. 5. Apsidal precession due to tidal distortion (solid-red-line) and general relativistic (GR) effects (dotted-blue-line) in a system composed by a $1 M_{\oplus}$ planet around a $0.08 M_{\odot}$ BD with initial $a = 0.01 \text{ au}$ and $e = 0.1$. In this example, the argument of periastron complete an orbit in $\sim 14750 \text{ yr}$ when is affected by GR and in $\sim 3060 \text{ yr}$ when is affected by tidal distortion.

then $\Omega_{\text{p}} = n$ so this time when $a = r_{\text{corot}}$ the planet starts moving outwards because $P_{\star} < P_{\text{p}}$.

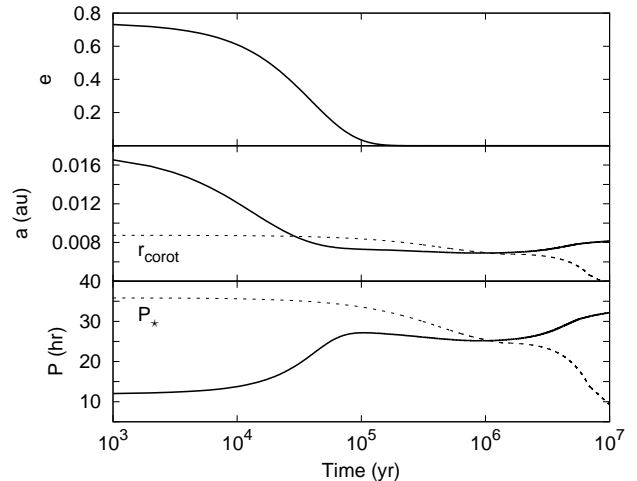


Fig. 6. Evolution of the e , a and the pseudo-synchronization period of a $1 M_{\oplus}$ around a $0.04 M_{\odot}$ BD. Solid lines indicates the results considering the initial orbital elements from Bolmont et al. (2011). The dashed-lines indicate the evolution of r_{corot} (mid panel) and the rotational period of the BD, P_{\star} (bottom panel).

5.4. N -body simulations

We performed 20 N -body simulations using the modified version of `MERCURY` code. We developed 10 simulations for the scenario *S1* and 10 simulations for the scenario *S2* as explained in Section 4.3.

We also run 10 simulations for each scenario described above using the original version of `MERCURY` code, without including external forces, in order to evaluate the relevance of tidal and general relativistic effects.

5.4.1. Protoplanetary embryo distributions

For using `MERCURY` code, it is necessary to give physical and orbital parameters for the protoplanetary embryos. We modeled the initial mass distributions of embryos as a function of the radial distance from the central object, which are initial conditions for our numerical simulations. The initial spatial distribution of protoplanetary embryos was computed following Eq. (4), considering a distance range $0.015 < r/\text{au} < 1$ and defining 1 Myr as the initial time. We considered that at such age the gas has been already dissipated from the disk.

Even though we are aware of the existence of a number of BDs which are still accreting gas from their disks up to ~ 10 Myr (references therein Pascucci et al. 2009; Downes et al. 2015, i.e.), the incorporation of the gas component is out of the scope of the present work which, in any case, reproduces those observed BDs that are not showing gas signatures at ~ 1 Myr.

We calculated the mass of each protoplanetary embryo M_p considering that at the initial time they are at the end of the oligarchic growth stage, having accreted all the planetesimals in their feeding zones (Kokubo & Ida 2000) by

$$M_p = 2\pi r \Delta r_H \Sigma_s(r), \quad (21)$$

where Δr_H is the orbital separation between two consecutive embryos in terms of their mutual Hill radii r_H , with Δ being an arbitrary integer number, given by

$$r_H = r \left(\frac{2M_p}{3M_\star} \right)^{\frac{1}{3}}. \quad (22)$$

Replacing Eqs. (4) and (22) into Eq. (21), we obtain an expression for the mass of each protoplanetary embryo as a function of the radial distance in the disk mid-plane r , which is given by

$$M_p = \left(2\pi r^2 \Delta \Sigma_{0s} \eta_{\text{ice}} \left(\frac{2}{3M_\star} \right)^{\frac{1}{3}} \left(\frac{r}{r_c} \right)^{-\gamma} e^{-\left(\frac{r}{r_c}\right)^{2-\gamma}} \right)^{\frac{3}{2}}. \quad (23)$$

We located our first embryo at the inner radii of our region $r_1 = 0.015$ au. Then we calculated its mass using Eq. (23). For the reminding embryos, we proposed a separation of $10 r_H$ between them by fixing $\Delta = 10$ (Kokubo & Ida 1998).

Thus we calculated the initial positions r_{i+1} and masses $M_{p,i+1}$ for the embryos by

$$r_{i+1} = r_i + \Delta r_i \left(\frac{2M_i}{3M_\star} \right)^{\frac{1}{3}}, \quad (24)$$

$$M_{p,i+1} = \left(A \left(\frac{2}{3M_\star} \right)^{\frac{1}{3}} \left(\frac{r_{i+1}}{r_c} \right)^{-\gamma} e^{-\left(\frac{r_{i+1}}{r_c}\right)^{2-\gamma}} \right)^{\frac{3}{2}}, \quad (25)$$

for $i = 1, 2, \dots$ with $A = 2\pi r_{i+1}^2 \Delta \Sigma_{0s} \eta_{\text{ice}}$.

Using Eqs. (24) and (25) we arrived to the initial distributions of masses of the protoplanetary embryos as a function of the radial distance, which represents the semi-major axis, from the central object for both scenarios S1 and S2. In Fig. 7 we illustrated both distributions. The S1 (star dots) has a distribution of 224 embryos with a total mass $M_{pT} \sim 0.25 M_\oplus$ located along

the region of study. There are 210 of them distributed in the inner region up to the snowline with a total mass $\sim 0.06 M_\oplus$, while the remaining 14 embryos are distributed beyond the snowline and have a total mass $\sim 0.19 M_\oplus$. The S2 (circle dots) has a distribution of 74 embryos located along the region of study with a total mass $M_{pT} \sim 3 M_\oplus$. There are 69 of them distributed in the inner region up to the snowline with a total mass $\sim 0.72 M_\oplus$, while the remaining 5 embryos with a total mass of $\sim 2.25 M_\oplus$ are placed beyond the snowline up to 1 au. The red dots represent the embryos which are located inside r_{ice} while the blue dots represent embryos which are located beyond r_{ice} .

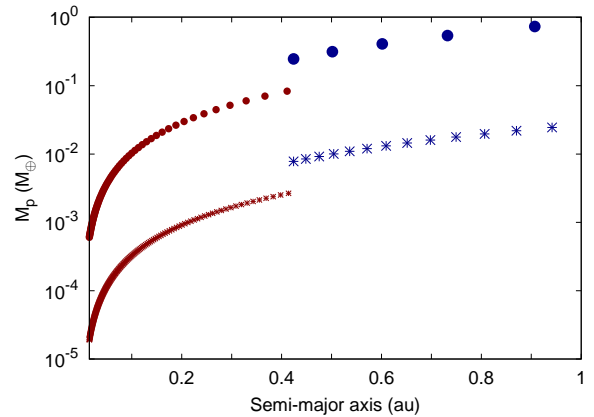


Fig. 7. Initial embryo distributions of masses as a function of their initial location given by their semi-major axis for S1 (circle dots) and S2 (star dots). The blue color represent the water-rich population (50% water in mass) while the red color represent the bodies with the lowest amount of water in mass (0.01%).

We considered lower values than 0.02 for the initial eccentricities and 0.5° for the initial inclinations. The regarding orbital elements, argument of periastron ω , longitude of the ascending node Ω and mean anomaly M are randomly determined, at the beginning of the simulations, between 0° and 360° from an uniform distribution for each protoplanetary embryo.

5.4.2. N -body code: characterization

For developing our simulations, we chosen the hybrid integrator, which uses a second order symplectic algorithm to treat interactions between objects with separations greater than 3 Hill radii and the Bulirsch-Stöer method for resolving closer encounters. The collisions are treated as perfectly inelastic ones, conserving the mass and the corresponding water content of protoplanetary embryos. We considered that a body is ejected from the system when it reaches a distance $a > 100$ au.

We adopted a time step of 0.08 days which corresponds to $1/30$ th of the orbital period of the innermost body in the simulations. In order to avoid any numerical error for small-perihelion orbits, we assumed $R_\star = 0.004$ au which corresponds to the maximum value of the radius of the central object.

All simulations were integrated over 100 Myr, which is a standard time for studying the dynamical evolution of planetary systems. Because of the stochastic nature of the accretion process between the protoplanets and, eventually with the main object, we remark that it is necessary to carry out a set of N -body simulations. In this case, we performed 10 simulations for each scenario which required a mean CPU time of six months on 3.6 GHz processors.

6. Results

In this section we present the resulting planetary systems of our simulations made in scenarios S1 and S2. We compare the resulting planets from simulations that included tidal and GR effects with those from simulations that neglected these effects to test their relevance during rocky planet formation. In particular we focus our analysis in the close-in population to the central object.

6.1. Planetary architectures

Our simulations predict a diversity of final planetary systems architectures at 100 Myr regarding all the simulations made in both scenarios. The Fig. 8 shows the final location of the resulting planetary systems of each simulation in scenario S1, regarding the final masses and fraction of water in mass. The planetary masses are between $0.01 M_{\oplus}$ and $0.12 M_{\oplus}$ (this means of the order of the mass of the *Moon* and the mass of *Mars* respectively) and the fraction of water in mass between 0.01% and 50%. The left panel shows the planetary architectures from simulations that included tidal and GR effects and the right panel their counterparts in the simulations that neglecting these effects. In both panels, the IHZ of the system at 100 Myr (cream band) and at 1 Gyr (pink band) are overlapped. In Fig. 9 we show the resulting architectures of the simulations for the scenario S2. The resulting planets have a range of masses between $0.2 M_{\oplus}$ and $1.8 M_{\oplus}$ and a percentage of water in mass between 0.01% and 50%.

The main difference we found is the close-in planet population that survived in the simulations that included tidal and GR effects, which did not survive in the simulations that neglected these effects. This fact becomes more relevant in S1, where the protoplanetary embryos involved were an order of magnitude less massive than in S2.

In the simulations made in S2, the embryos involved suffered stronger gravitational interactions between them than those from S1 because they are more massive bodies. Thus generate more excitation in the system allowing some embryos to collide with the central object and to be ejected from the system. This interactions became more relevant than tidal and GR effects for the very close-in body population in S2. This is supported by the percentage of embryos that have collided with the central object or ejected from the system (reached $a > 100$ au) as shown in Fig. 10. The percentage is given over the initial amount of embryos in each scenario of work: 224 embryos in S1 and 74 embryos in S2. The blue bars represent the percentage of those embryos from simulations where tidal and GR effects are included and red bars those from simulations where these effects are neglected. It can be seen that the amount of bodies that either have collided with the central object or have been ejected from the system in S2 is much higher than in S1 because of the higher level of excitation of the system. Moreover, the simulations that included tidal and GR effects reduced the collisions of embryos with the central object and had almost no impact in the ejection of embryos because at long distances from the central object tidal effects became irrelevant.

By compacting all the resulting planetary systems in Fig. 11, we represent their distribution in a regarding their masses for S1 (top panel) and S2 (bottom panel). The IHZ at 100 Myr and at 1 Gyr are overlapped as well in cream and pink color bands respectively. The blue dots represent resulting planets formed while including tidal and GR effects and red dots represent those formed neglecting these effects. The surviving close-in body population has low masses and is mainly resulting from simu-

lations with tidal and GR effects from S1. Thus the relevance of tidal and GR effects depends also on the mass of the bodies involved in the simulations.

The Fig. 12 shows the eccentricities of the resulting planets as a function of their semi-major axis for S1 (top panel) and S2 (bottom panel). It seems that low-mass and close-in planets that survived while including external effects have non neglecting eccentricities. This is because the many gravitational interactions between embryos produce excitation in their orbital parameters and the timescale for eccentricity damping which is much larger (\sim Gyr) than the integration time of our simulations. As we discussed in previous sections, tidal effects added in our simulations affect the distribution of eccentricities and semi-major axis of the resulting planets but the long decay timescales do not let us see the damping in e yet. Nevertheless, the e damping will be efficient by the time the central object reaches 1 Gyr old for the planets that remind located close-in to the central object, where the IHZ will be located by that time.

Our results strongly suggest that a formation scenario where tidal and GR effects are included is a more realistic scenario for planet formation at the sub-stellar mass limit. We remark that even though, GR corrections are relevant during planet formation to map more realistic orbits and therefore more realistic encounters between embryos, are the tidal effects which play a primary role in the survival of an in-situ population. However, when the masses of the bodies involved increase (like in S2) tidal effects became less relevant than gravitational interactions between them (see Section 7).

6.2. The water mass fraction

Both scenarios shows a diversity regarding the fraction of water in mass, but always the resulting planets inside $a < 0.1$ au conserved this initial fraction of water in mass, that we assumed to be 0.01% of the mass of embryos located inside the snowline at the beginning of the simulations.

For S1, planets at $a > 0.1$ au present a range in percentage of water in mass which is between 10% and 35%, for planets with semi-major axis $0.1 < a/\text{au} < 0.42$, and is between 35% and 50% for planets with $0.42 < a/\text{au} < 1$. The outer-water-rich planets keep their high content of water in mass and an intermediate population of water-rich resulting planets appears close to location of the snowline.

For S2, planets at $a > 0.1$ au only present a high mass percentage of water, between 35% and 50%. Embryos located outside the snowline either have suffered impacts for other water-rich bodies or have been ejected from the system, not giving place to an intermediate water-rich population as in S1.

In order to explain the origin of the resulting distribution of water of the surviving planets in our region of study, in the next Section we analyze their whole collisional history.

6.3. Collisional history

During the first 100 Myr of planet formation that we studied in our simulations, embryos had gravitational interactions suffering encounters and collisions between them. Regarding its initial location in the system, each embryo can interact with others that have different orbital and physical parameters around its gravitational influence zone. As the N -body code is treating all collisions as perfect inelastic ones, after two bodies collided the resulting body will be a merge of the initial two.

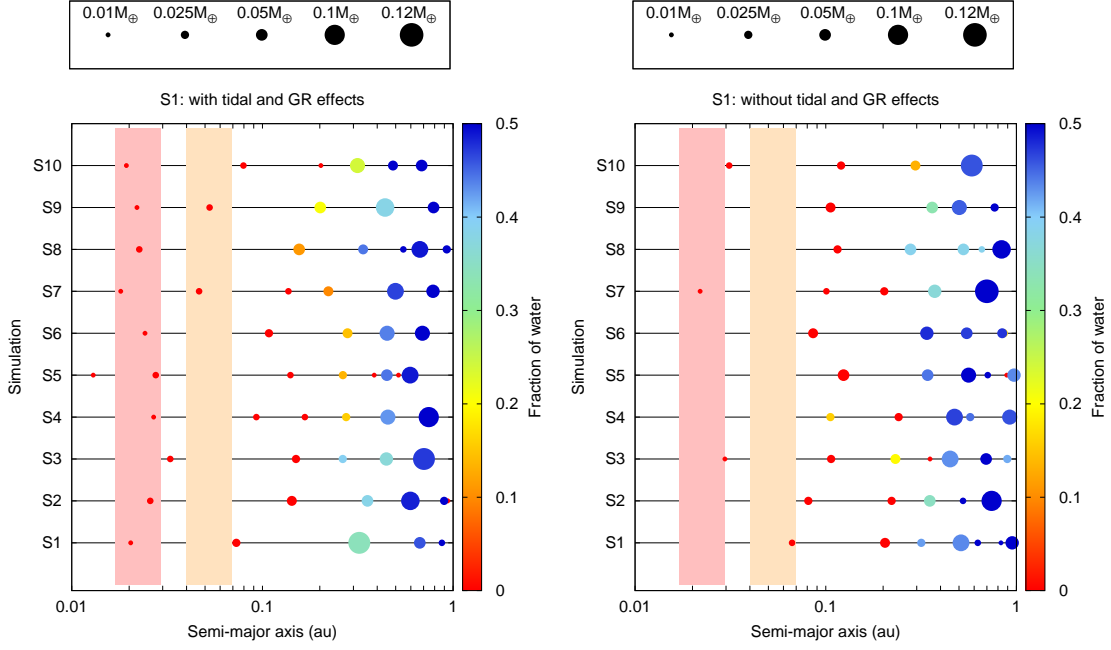


Fig. 8. Distribution of the resulting planets locations in the region of study in each simulation for the scenario S1. Planets were discriminated by mass and fraction of water in mass. Masses of the resulting planets are shown at the top of each graphic, having a range between $0.01 M_{\oplus}$ and $0.12 M_{\oplus}$ (this means of the order of the mass of the *Moon* and the mass of *Mars* respectively). The fraction of water in mass is presented in a color-scale and assigned to each body in a percentage between 0.01% and 50%. The left panel represents the resulting planets from simulations in which tidal and GR effects are included along the integration time while the right panel represents those planets from simulations that neglected these effects. The cream band represent the IHZ at 100 Myr while the pink band the IHZ at 1 Gyr.

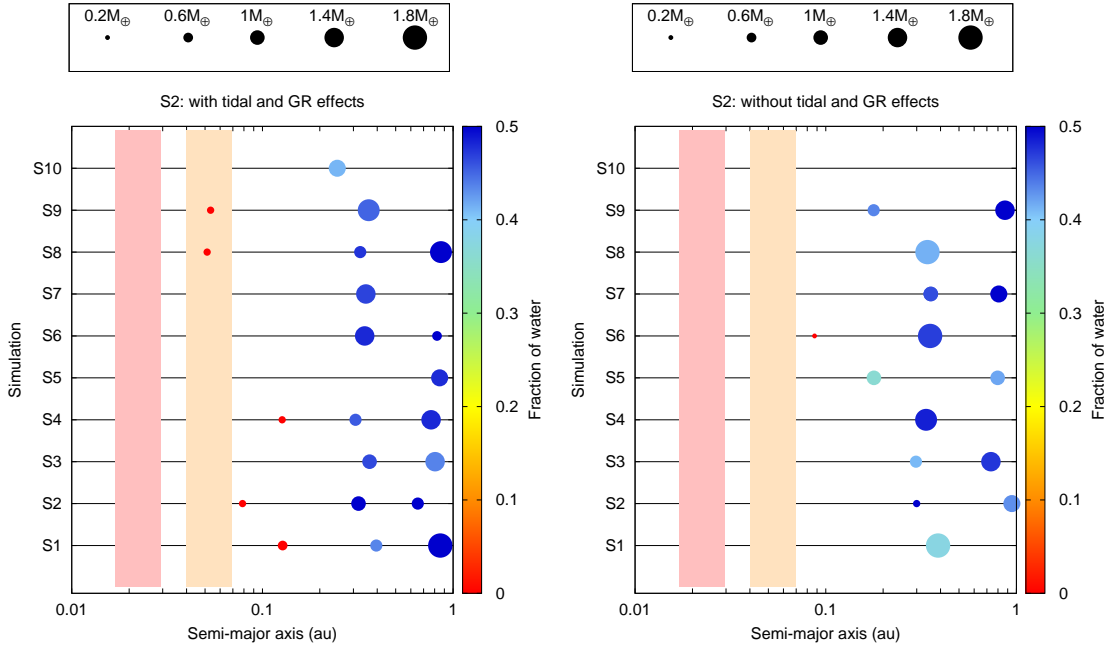


Fig. 9. Distribution of the resulting planet locations in the region of study in each simulation for the scenario S2. The mass range of the resulting planets is between $0.2 M_{\oplus}$ and $1.8 M_{\oplus}$. The color characterization is the same as in Fig 8.

From the previous analysis regarding the final distributions of the resulting planets and their final fraction of water in mass we can discriminate different sub-regions for studying the collisional history of the resulting planets: an inner region of planets finally located at $a < 0.1$ au, an intermediate region, between $0.1 < a/\text{au} < 0.42$ and an outer region beyond the snowline between $0.42 < a/\text{au} < 1$.

The Fig. 13 shows the collisional history of all the resulting planets of S1 when tidal and GR effects are included (top panel) and when these effects are neglected (bottom panel). The red lines represent the resulting planets finally located in the inner region, the orange ones the planets in the intermediate region and the blue lines, those in the outer region. Each peak represents the initial location of the embryo that collided with the resulting

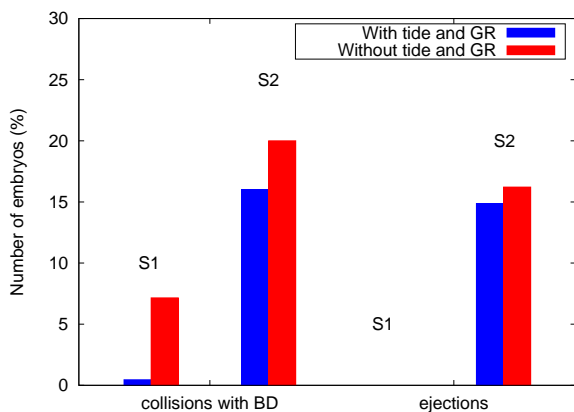


Fig. 10. Percentage of embryos that had collided or had been ejected from the system along the integration time of each scenario of work. Blue bars correspond to embryos from simulations that included tidal and GR effects while red bars represent embryos from simulations that neglected these effects.

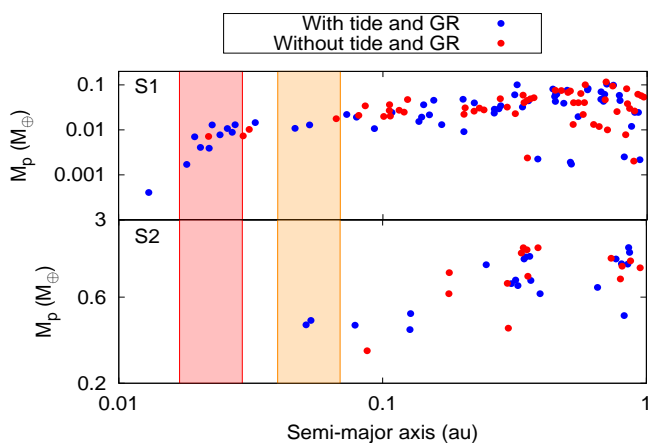


Fig. 11. Distribution in mass of the resulting planets regarding their semi-major axis at 100 Myr in S1 (top panel) and S2 (bottom panel). Blue dots represent resulting planets from simulations that included tidal and GR effects while red dot represent those ones from simulations that neglected these effects. The pink band represents the location of the IHZ at 1 Gyr while the cream band represent its location at 100 Myr.

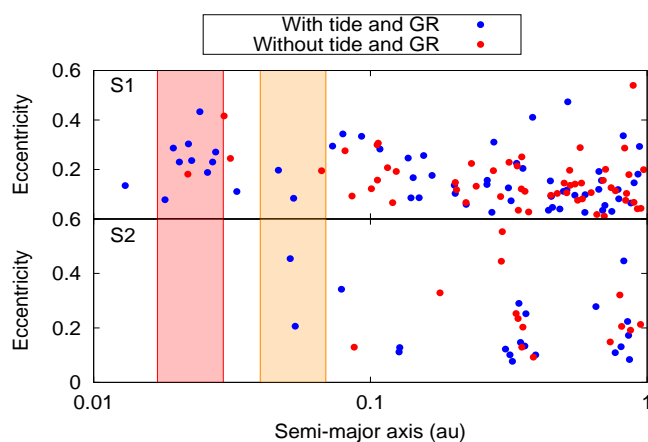


Fig. 12. Orbital distribution of the resulting planets regarding their location in the system and eccentricity in S1 (top panel) and S2 (bottom panel). Colors are as in Figure 11.

planet and the percentage of mass that it added to the planet after the perfect collision. In the inner region the resulting planets have collided with embryos initially located at $a < 0.35$ au (both in top and bottom panel), all located inside the snowline which make them preserve the initial fraction of water in mass. In the intermediate region planets have accreted embryos initially located between $0.05 < a/\text{au} < 0.88$ (top panel) and between $0.05 < a/\text{au} < 0.95$ (bottom panel), which explain the intermediate range of fraction of water in mass after collided with embryos inside and outside the snowline. Finally, in the outer region planets have collided with embryos initially located between $0.2 < a/\text{au} < 0.95$ (top panel) and $0.22 < a/\text{au} < 0.95$ (bottom panel). In this outer region, even though the resulting planets suffered collisions with embryos distributed along a wide range of the system, just few planets located inside the snowline collided with such planets, thus they maintain huge fraction of water in mass. It is important to remark that the close-in population located at $a < 0.1$ au did not collide with other embryos beyond this semi-major axis when tidal effects were included in the simulations.

On the other hand, the Fig. 14 shows the collisional history of the resulting planets of S2 when tidal and GR effects are included (top panel) and when these effects are neglected (bottom panel). The color of the lines represents the same as in Fig. 13. In this case, in the inner region planets have collided with embryos initially located at $a < 0.36$ au (top panel) and $a < 0.22$ au (bottom panel). In the intermediate region planets have accreted embryos initially located between $0.06 < a/\text{au} < 0.72$ (top panel) and $0.07 < a/\text{au} < 0.91$ (bottom panel). Finally, in the outer region planets have collided with embryos initially located at $0.17 < a/\text{au} < 0.72$ (top panel) and $0.097 < a/\text{au} < 0.72$. In S2, planets in the intermediate and outer region accreted material from a similar region, with few embryos initially located inside the snowline. Thus all those planets retained huge amount of water in mass. In this case the three planets that survived with at $a < 0.1$ au did not collide with other embryos beyond this semi-major axis as it happened in S1 when tidal effects were included in the simulations.

The collisional history of the resulting planets explains their final masses and fraction of water in mass. Moreover, it allows us to conclude that the close-in surviving population which was the most affected one by tidal effects just suffered collisions with the close-in initially located embryos.

6.4. Close-in population: potentially habitable planets

We focus our analysis in the close-in bodies that survived in the simulated planetary systems because they are candidates to be potentially habitable planets.

6.4.1. Characterization

Inside the location of the IHZ at 100 Myr (final time of simulations), in S1 two planets reminded when tidal and GR effects are included in the simulations and just one planet when these effects are not included in the simulations regarding their semi-major axis. On the other hand, in S2 two planets reminded in the IHZ when external effects are included and no candidate survived when these effects are neglected in the simulations. Moreover, if we consider the value of the eccentricity and we calculate periastron distance (q) and apoastro distance (Q) of those planets, just 1 planet reminded inside the IHZ regarding a , q and Q

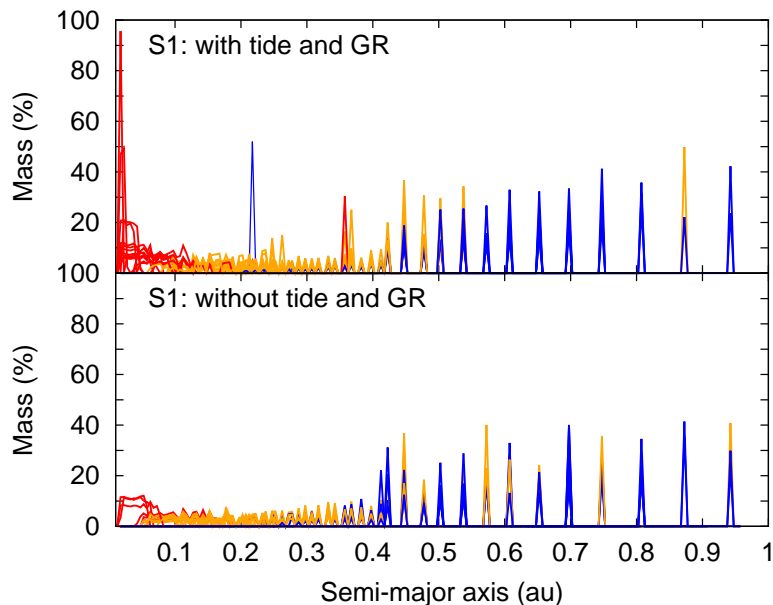


Fig. 13. Collisional history of the resulting planets from the simulations made in S1 in which tidal and GR effects are included (top panel) and in which these effects are neglected (bottom panel). Each jump in semi-major axis indicates the initial location of the embryo that collided with the resulting planets that increases their masses a given percentage after the perfect merge. The red lines indicate the history of the resulting planets finally located at $a < 0.1$ au, the orange lines planets located at $0.1 < a/\text{au} < 0.42$ and the blue lines planets located at $0.42 < a/\text{au} < 1$.

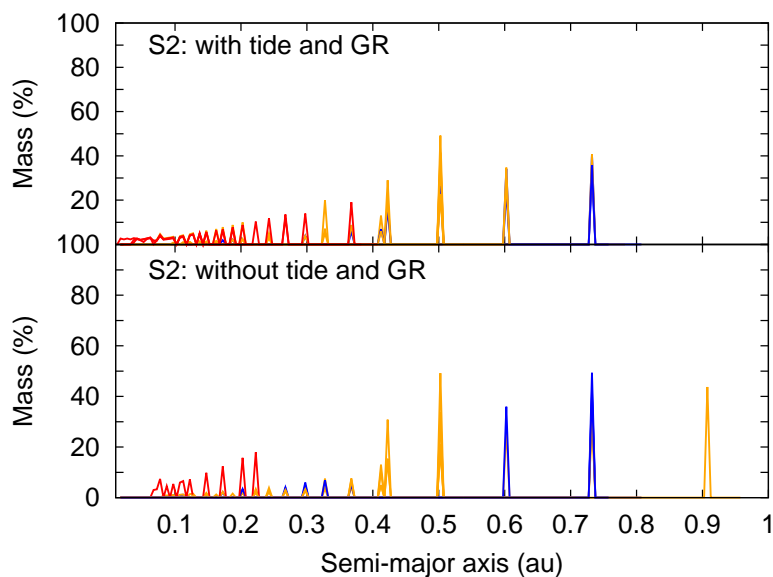


Fig. 14. Collisional history of the resulting planets from the S2 simulations in which tidal and general relativistic effects are included (top panel) and in which these effects are neglected (bottom panel). Colors are as in Fig. 13.

in S1 and 1 in S2 when considering tidal and general relativistic effects in the simulations.

In Section 3 we discussed the behavior of IHZ around very low-mass stars which is located close to the star and evolves towards smaller radius as the star evolves with time. Thus why we extended our analysis to those bodies that ended up closer-in to the central object, in particular, inside the location of the IHZ at 1 Gyr. The S1 was the only that generated such a close-in body population: 9 planets when including tidal and GR effects and just 1 when these effects are neglected in the simulations regarding their semi-major axis. Even though we do not have the orbital

parameters at 1 Gyr, it is expected that the eccentricities of those planets will be small enough to remind in the IHZ at 1 Gyr in S1 (see Section 5).

In Table 1 we present some physical parameters of the resulting planets that remind located at the IHZ at 100 Myr or at 1 Gyr in both scenarios of work.

We remark then that S1 when tidal and GR effects are included in the simulations, is the most favorable scenario to allow such candidates of potentially habitable planets, (see Section 7 for further discussion.)

Scenario	Embryo	a [au]	e	M [M_{\oplus}]	H_2O [%]	IHZ
S1t	39	0.020	0.23	0.004	0.01	b
S1t	132	0.025	0.18	0.010	0.01	b
S1t	113	0.026	0.23	0.008	0.01	b
S1t	113	0.027	0.27	0.013	0.01	b
S1t	132	0.024	0.43	0.007	0.01	b
S1t	33	0.018	0.07	0.001	0.01	b
S1t	126	0.046	0.19	0.010	0.01	a
S1t	115	0.022	0.23	0.013	0.01	b
S1t	63	0.022	0.30	0.006	0.01	b
S1t	142	0.052	0.08	0.013	0.01	a
S1t	62	0.019	0.28	0.007	0.01	b
S1wt	163	0.066	0.195	0.017	0.01	a
S1wt	90	0.022	0.18	0.007	0.01	b
S2t	59	0.051	0.45	0.337	0.01	a
S2t	39	0.053	0.20	0.370	0.01	a

Table 1. Potentially habitable planets from both scenarios when tidal and GR effects are included in the simulations (S1t and S2t) and when these effects are neglected in the case of S1 (S1wt). The initial numbers of the embryo that becomes the resulting planet in column 2 with their respectively final semi-major axis, eccentricity, mass and percentage of water in mass. Regarding its final location, the planets are located in the IHZ at 100 Myr (IHZ = a) or in the IHZ at 1 Gyr (IHZ = b).

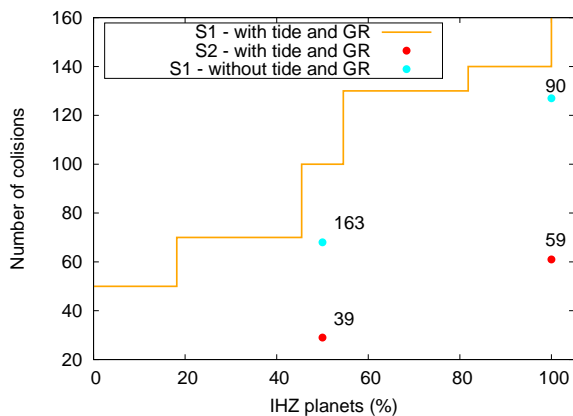


Fig. 15. Cumulative collisions between the resulting planets that survived inside both IHZ at 100 Myr and at 1 Gyr for S1 with tide and GR (orange line), S1 without considering tide or GR (cyan-dots) and S2 with tide and GR (red-dots).

6.4.2. Mass accretion history

All the close-in population that we consider as candidates to potentially habitable planets experienced a strong collisional history along the integration time of our simulations. All of them were targets of a high amount of impacts. In Fig. 15 the number of collisions that suffered all the IHZ candidates at 100 Myr and 1 Gyr is shown in orange color while the 2 planets that survived in S1 without considering tidal and GR effects are cyan-dots and the 2 that survived in S2 with these effects included are red-dots. In S1, all the resulting planets received more than 50 impacts and a maximum of 160 impacts with 50% of the total that received more than 100 impacts when tidal and GR effects were included, while the planets received 70 and 127 impacts, respectively, when these effects are neglected. In S2, one of the planets received 29 impacts while the other one almost 70 impacts, when tidal and GR effects were included. Each impact corresponds to a collision with an other embryo of the simulation. In S1 more im-

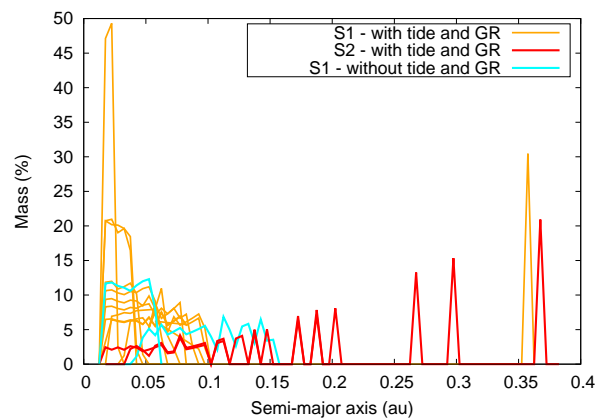


Fig. 16. Initial location of each embryo that collided with planets that survived inside the IHZ at 100 Myr or 1 Gyr related with the percentage of mass that the candidate planet obtain after each collision in S1 with tide and GR (orange curves), in S2 without tide and GR (cyan curves) and in S2 with tide and GR (red curves).

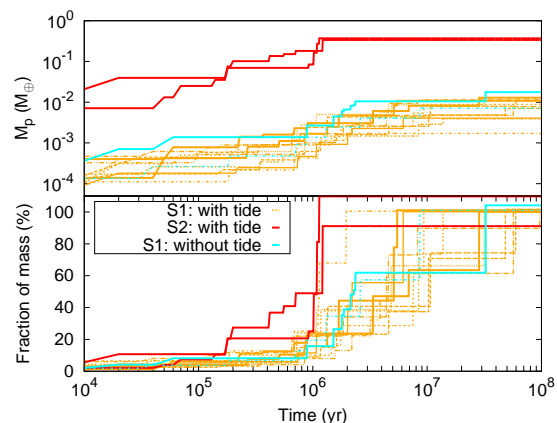


Fig. 17. Evolution of the mass (top panel) and its fraction with respect to the final mass (bottom panel) of the resulting planets that survived inside the IHZ at 100 Myr (solid-lines) and 1 Gyr (dotted-lines) in S1 with tide and GR (orange curves), in S2 without tide and GR (cyan curves) and in S2 with tide and GR (red curves).

pacts are allowed because the total amount of embryos is much higher (224 in total) than in S2 (74 in total). In any case, all the candidate planets collided with between 25% and 50% of the total number of embryos during this first 100 Myr of their evolution.

As it is shown in Table 1 all the planets inside both IHZ conserved their initial fraction of water in mass. This is because all the impacts that they suffered came from embryos located inside the snowline of the system. The Fig. 16 shows the location in semi-major axis of each embryo that collided with one IHZ candidate related with the percentage of mass that the candidate obtained after each collision in S1 with tide and GR (orange curves), in S2 without tide and GR (cyan curves) and in S2 with tide and GR (red curves). This figure is a zoom of Fig. 13 (both panels) and Fig. 14 (top panel) for the planets located in both determined IHZ.

The impacts that each body suffered during the integration time produced always an increase in mass because the N-body code used to develop the simulations considers all collisions as completely inelastic ones so every time a collision between embryos occurs is ending up in a perfect merge (see Section 7).

In Fig 17 we show the evolution in mass of each IHZ candidate planet (top panel) and its fraction of mass (bottom panel) following the same pattern of color as in Fig. 16. Each step in the curves represent mass or fraction of mass, respectively, gained by the IHZ candidate planet after each collision. It can be seen that there is no difference in between candidate planets which ended located in the IHZ at 100 Myr (solid-lines) and 1 Gyr (dotted-lines) in each scenario of work with respect to the mass accretion history.

7. Conclusions and discussions

In this work we study the rocky planet formation around a star close to the sub-stellar mass limit by using N -body simulations which includes tidal and general relativity effects and do not include the effect of gas in the disk. Our aim was to evaluate the relevance of tidal effects following the equilibrium tidal model, during the formation and evolution of the system and improve the accuracy in the calculation of the orbit of the protoplanetary embryos by considering general relativistic effects.

The equilibrium tide model used in this work is based on the assumption that when a star suffers the tidal disturbance from a companion body it instantly adjusts to hydrostatic equilibrium (Darwin 1879). A more general approach must include the dynamical tide model for a more reliable description of the very high eccentricity orbits as shown by Ivanov & Papaloizou (2011) and references therein. As shown in Figure 10, the simulations which do not include tides have 7% and 20% of embryos colliding with the central star in S1 and S2 respectively due to their high eccentricity. When tides are included through the equilibrium model these fractions change respectively to 1% and 16%. New simulations including the dynamical tide model are needed in order to explore the possible change in these fractions, which we expect to occur towards lower values due to the stronger tidal damping produced by this model.

Using a different model for close-in bodies, Makarov & Efroimsky (2013) found non pseudo-synchronization in the rotational periods for terrestrial planets and moons. In our case, we adopted the pseudo-synchronization in order to keep consistency with the Hut (1981) model adopted for the N -body simulations because the hypothesis of pseudo-synchronization is a direct consequence of the constant time-lag model (Darwin 1879; Hut 1981; Eggleton et al. 1998). A comparative analysis of our results with those from other treatments as well as the self-consistent inclusion of the rotational evolution of embryos is behind the goals of this work.

Because of the current uncertainties in the determination of disk masses, the simulations were performed for two different scenarios S1 and S2 which basically differ in the initial mass of solid material in the disk, $\sim 3 M_{\oplus}$ and $\sim 30 M_{\oplus}$ respectively. These values roughly represent the corresponding upper and lower limits of the disc mass for stars close to the sub-stellar mass limit.

The resulting planets have masses between $0.01 < m/M_{\oplus} < 0.12$ in scenario S1 and $0.2 < m/M_{\oplus} < 1.8$ in scenario S2. Even though we used lower values for the mass of the disk than those from Payne & Lodato (2007), we found the same correlation between the resulting planet masses and the initial amount of solid material in the disk. In fact, when the mass of the disk increases, more massive planets could be formed.

When tidal and general relativistic effects are included, in scenario S1 a close-in planetary population located at $a < 0.07$ au survived in all the simulations while in the more massive

scenario S2 embryos suffered stronger gravitational interaction and the formation of such close-in population occurs only in 2 of the 10 simulations. This is why our S1 is the most favorable scenario to generate close-in planets. Then, we found that tidal and general relativistic effects are relevant during the formation and evolution of rocky planets around an object at the sub-stellar mass limit, in particular when the protoplanetary embryos involved are low-mass bodies. Our work together with the model developed by Bolmont et al. (2011, 2013, 2015) show the necessity of including tidal effects along both the formation and later evolution of such systems.

The close-in population resulted from a large number of collisions within protoplanetary embryos which has been treated in our simulations as perfectly inelastic ones. It gives upper limits in the final value of mass and water content for the resulting planets. Thus why it is necessary to reproduce the simulations by using a N -body code that includes fragmentation during collisions which can decrease considerably the final masses of the resulting planets as shown by Chambers (2013); Dugaro et al. (2019).

The close-in population found have a particular interest because is located inside the evolving IHZ of the system. We classify a set of 15 close-in bodies as candidates to potentially habitable planets only on the basis of their semi-major axes and eccentricities. A complete analysis of their probability of being habitable planets considering additional constraints (e.g. Martin et al. 2006) is beyond the scope of this work.

Our model presents an important improvement in the scenario of rocky planet formation at the sub-stellar mass limit by including tidal and general relativistic effects. We stress that, even though Coleman et al. (2019) did not incorporate these effects on their simulations of planet formation around Trappist-1, they shown the relevance of considering the gas component of the disk during the first 1 Myr. Then, clearly a more realistic simulation of this scenario of planet formation must include all these effects. A new set of such N -body simulations considering low-mass stars and BDs as central objects, with different masses is currently ongoing.

We conclude that tidal and general relativistic effects are relevant during rocky planet formation at the sub-stellar mass limit because they allow the survival of close-in bodies located inside the IHZ. It supports these systems as important candidates for future searches of life in the solar neighborhood.

Acknowledgements. This work was partially financed by Agencia Nacional de Promoción Científica y Tecnológica (ANPCyT) through PICT 201-0505, and by Universidad Nacional de La Plata (UNLP) through PID G144. We acknowledge the financial support by Facultad de Ciencias Astronómicas y Geofísicas de La Plata (FCAGLP) and Instituto de Astrofísica de La Plata (IALP) for extensive use of their computing facilities. We specially appreciate the kind support and advice from Bolivia Cuevas-Otahola (INAOE, México) during the numerical simulations and Adrián Rodríguez Colucci (UFRJ, Brazil) for his valuable comments. We thank the editor Benoît Noyelles and the anonymous referee for very valuable suggestions which helped improve the presentation of our results.

References

- Anderson, J. D., Esposito, P. B., Martin, W., Thornton, C. L., & Muhleman, D. O. 1975, *ApJ*, 200, 221
- Andrews, S. M., Wilner, D. J., Hughes, A. M., Qi, C., & Dullemond, C. P. 2009, *The Astrophysical Journal*, 700, 1502
- Andrews, S. M., Wilner, D. J., Hughes, A. M., Qi, C., & Dullemond, C. P. 2010, *ApJ*, 723, 1241
- Andrews, S. M., Wilner, D. J., Hughes, A. M., Qi, C., & Dullemond, C. P. 2010, *The Astrophysical Journal*, 723, 1241
- Baraffe, I., Homeier, D., Allard, F., & Chabrier, G. 2015, *A&A*, 577, A42
- Barclay, T., Pepper, J., & Quintana, E. V. 2018, *The Astrophysical Journal Supplement Series*, 239, 2

- Barnes, R., Mullins, K., Goldblatt, C., et al. 2013, *Astrobiology*, 13, 225
- Barnes, R., Raymond, S. N., Greenberg, R., Jackson, B., & Kaib, N. A. 2010, *ApJ*, 709, L95
- Bastian, N., Covey, K. R., & Meyer, M. R. 2010, *ARA&A*, 48, 339
- Beaugé, C. & Nesvorný, D. 2012, *ApJ*, 751, 119
- Benitez, F. & Gallardo, T. 2008, *Celestial Mechanics and Dynamical Astronomy*, 101, 289
- Bolmont, E., Raymond, S. N., & Leconte, J. 2011, *A&A*, 535, A94
- Bolmont, E., Raymond, S. N., Leconte, J., Hersant, F., & Correia, A. C. M. 2015, *A&A*, 583, A116
- Bolmont, E., Selsis, F., Raymond, S. N., et al. 2013, *A&A*, 556, A17
- Chambers, J. E. 1999, *MNRAS*, 304, 793
- Chambers, J. E. 2013, *Icarus*, 224, 43
- Chiang, E. I. & Goldreich, P. 1997, *ApJ*, 490, 368
- Ciesla, F. J., Mulders, G. D., Pascucci, I., & Apai, D. 2015, *ApJ*, 804, 9
- Coleman, G. A. L., Leleu, A., Alibert, Y., & Benz, W. 2019, arXiv e-prints, arXiv:1908.04166
- Cumming, A., Butler, R. P., Marcy, G. W., et al. 2008, *PASP*, 120, 531
- Darwin, G. H. 1879, *Philosophical Transactions of the Royal Society of London Series I*, 170, 1
- Darwin, G. H. 1908, *Proceedings of the Royal Society of London Series A*, 80, 166
- Downes, J. J., Román-Zúñiga, C., Ballesteros-Paredes, J., et al. 2015, *MNRAS*, 450, 3490
- Dugaro, A., de Elía, G. C., & Darriba, L. A. 2019, arXiv e-prints, arXiv:1910.02982
- Eggleton, P. P., Kiseleva, L. G., & Hut, P. 1998, *ApJ*, 499, 853
- Einstein, A. 1916, *Annalen der Physik*, 354, 769
- Gillon, M., Triaud, A. H. M. J., Demory, B.-O., et al. 2017, *Nature*, 542, 456
- Grimm, S. L., Demory, B.-O., Gillon, M., et al. 2018, *A&A*, 613, A68
- Guilloteau, S., Dutrey, A., Piétu, V., & Boehler, Y. 2011, *A&A*, 529, A105
- Hansen, B. M. S. 2010, *ApJ*, 723, 285
- Hardegree-Ullman, K. K., Cushing, M. C., Muirhead, P. S., & Christiansen, J. L. 2019, *The Astronomical Journal*, 158, 75
- Hartmann, L., Calvet, N., Gullbring, E., & D'Alessio, P. 1998, *ApJ*, 495, 385
- Hayashi, C. & Nakano, T. 1963, *Progress of Theoretical Physics*, 30, 460
- He, M. Y., Triaud, A. H. M. J., & Gillon, M. 2017, *Monthly Notices of the Royal Astronomical Society*, 464, 2687
- Heller, R., Jackson, B., Barnes, R., Greenberg, R., & Homeier, D. 2010, *A&A*, 514, A22
- Hendler, N. P., Mulders, G. D., Pascucci, I., et al. 2017, *ApJ*, 841, 116
- Henry, T. J. 2004, in *Astronomical Society of the Pacific Conference Series*, Vol. 318, *Spectroscopically and Spatially Resolving the Components of the Close Binary Stars*, ed. R. W. Hilditch, H. Hensberge, & K. Pavlovski, 159–165
- Herbst, W., Eislöffel, J., Mundt, R., & Scholz, A. 2007, in *Protostars and Planets V*, ed. B. Reipurth, D. Jewitt, & K. Keil, 297
- Hojjatpanah, S., Figueira, P., Santos, N. C., et al. 2019, arXiv e-prints, arXiv:1908.04627
- Howard, A. W. 2013, *Science*, 340, 572
- Hut, P. 1981, *A&A*, 99, 126
- Isella, A., Carpenter, J. M., & Sargent, A. I. 2009, *ApJ*, 701, 260
- Ivanov, P. B. & Papaloizou, J. C. B. 2011, *Celestial Mechanics and Dynamical Astronomy*, 111, 51
- Kasting, J. F. 1988, *Icarus*, 74, 472
- Kasting, J. F., Whitmire, D. P., & Reynolds, R. T. 1993, *Icarus*, 101, 108
- Kobayashi, H., Kimura, H., Watanabe, S.-i., Yamamoto, T., & Müller, S. 2011, *Earth, Planets, and Space*, 63, 1067
- Kokubo, E. & Ida, S. 1998, *Icarus*, 131, 171
- Kokubo, E. & Ida, S. 2000, *Icarus*, 143, 15
- Kopparapu, R. K., Ramirez, R., Kasting, J. F., et al. 2013a, *ApJ*, 770, 82
- Kopparapu, R. K., Ramirez, R., Kasting, J. F., et al. 2013b, *ApJ*, 765, 131
- Kubas, D., Beaulieu, J. P., Bennett, D. P., et al. 2012, *A&A*, 540, A78
- Kumar, S. S. 1963, *ApJ*, 137, 1121
- Leconte, J., Chabrier, G., Baraffe, I., & Levrard, B. 2010, *A&A*, 516, A64
- Lodders, K. 2003, *ApJ*, 591, 1220
- Lodders, K., Palme, H., & Gail, H.-P. 2009, *Landolt Börnstein* [arXiv:0901.1149]
- Lovis, C., Snellen, I., Mouillet, D., et al. 2017, *Astronomy and Astrophysics*, 599, A16
- Luhman, K. L. 2012, *ARA&A*, 50, 65
- Lynden-Bell, D. & Pringle, J. E. 1974, *MNRAS*, 168, 603
- Makarov, V. V. & Efrogmsky, M. 2013, *ApJ*, 764, 27
- Manara, C. F., Morbidelli, A., & Guillot, T. 2018, *Astronomy and Astrophysics*, 618, L3
- Martin, H., Albarède, F., Claeys, P., et al. 2006, *Earth Moon and Planets*, 98, 97
- Miguel, Y., Cridland, A., Ormel, C. W., Fortney, J. J., & Ida, S. 2019, arXiv e-prints, arXiv:1909.12320
- Mohanty, S., Basri, G., Shu, F., Allard, F., & Chabrier, G. 2002, *ApJ*, 571, 469
- Mordasini, C., Alibert, Y., & Benz, W. 2009, *A&A*, 501, 1139
- Mulders, G. D., Pascucci, I., & Apai, D. 2015, *IAU General Assembly*, 22, 2256025
- Neron de Surgy, O. & Laskar, J. 1997, *A&A*, 318, 975
- Padoan, P. & Nordlund, Å. 2004, *ApJ*, 617, 559
- Papaloizou, J. C. B. & Terquem, C. 2010, *MNRAS*, 405, 573
- Pascucci, I., Apai, D., Luhman, K., et al. 2009, *ApJ*, 696, 143
- Payne, M. J. & Lodato, G. 2007, *Monthly Notices of the Royal Astronomical Society*, 381, 1597
- Pollack, J. B., Hollenbach, D., Beckwith, S., et al. 1994, *ApJ*, 421, 615
- Quinn, T. R., Tremaine, S., & Duncan, M. 1991, *AJ*, 101, 2287
- Ragazzoni, R., Magrin, D., Rauer, H., et al. 2016, in *Society of Photo-Optical Instrumentation Engineers (SPIE) Conference Series*, Vol. 9904, *Proc. SPIE*, 990428
- Raymond, S. N., Scalo, J., & Meadows, V. S. 2007, *ApJ*, 669, 606
- Ricci, L., Isella, A., Carpenter, J. M., & Testi, L. 2013, *The Astrophysical Journal*, 764, L27
- Ricci, L., Testi, L., Natta, A., Scholz, A., & de Gregorio-Monsalvo, I. 2012, *The Astrophysical Journal*, 761, L20
- Ricci, L., Testi, L., Natta, A., et al. 2014, arXiv.org, 20
- Ronco, M. P., Guilera, O. M., & de Elía, G. C. 2017, *MNRAS*, 471, 2753
- Scholz, A., Kostov, V., Jayawardhana, R., & Mužić, K. 2015, *ApJ*, 809, L29
- Selsis, F., Kasting, J. F., Levrard, B., et al. 2007, *A&A*, 476, 1373
- Shahid-Saless, B. & Yeomans, D. K. 1994, *AJ*, 107, 1885
- Sterne, T. E. 1939, *MNRAS*, 99, 451
- Testi, L., Natta, A., Scholz, A., et al. 2016, *A&A*, 593, A111
- Varadi, F., Runnegar, B., & Ghil, M. 2003, *ApJ*, 592, 620
- Walker, J. C. G., Hays, P. B., & Kasting, J. F. 1981, *J. Geophys. Res.*, 86, 9776
- Watson, A. J., Donahue, T. M., & Walker, J. C. G. 1981, *Icarus*, 48, 150
- Zanardi, M., de Elía, G. C., Di Sisto, R. P., & Naoz, S. 2018, *A&A*, 615, A21
- Zechmeister, M., Dreizler, S., Ribas, I., et al. 2019, *Astronomy and Astrophysics*, 627, A49

Appendix A: Snowline location at the sub-stellar regime

The snowline location corresponds to the radial distance to the central object where water condenses. This occurs when the partial pressure of the protoplanetary disk exceeds the saturation pressure. The exactly temperature where it occurs, depends on the physical structure of the disk and the relative abundances of elements, but is expected to be in a range between $140 < T/K < 170$. To determine the snowline location of a system with a sub-stellar object of a mass $0.08 M_{\odot}$ as a primary object, we took the same temperature profile of a disk which radiates as black body as Chiang & Goldreich (1997)

$$T(r) = T_{\star} \left(\frac{\alpha}{2}\right)^{\frac{1}{4}} \left(\frac{r}{R_{\star}}\right)^{-\frac{1}{2}}. \quad (\text{A.1})$$

The parameter α represents the glazing angle at which the starlight strikes the disk. In Chiang & Goldreich (1997), by considering vertical hydrostatic equilibrium, they arrived to the following expression

$$\alpha = \frac{0.4R_{\star}}{a} + a \frac{d}{da} \left(\frac{H}{a}\right), \quad (\text{A.2})$$

where the parameter H represents the height of the visible photosphere above the disk mid-plane and the factor (H/a) can be express by

$$\frac{H}{a} = 4T_{\star}^{\frac{4}{7}} R_{\star}^{\frac{2}{7}} \left(\frac{k}{GM_{\star}\mu_{\text{g}}}\right)^{\frac{4}{7}} a^{\frac{2}{7}}, \quad (\text{A.3})$$

where k is the Boltzman constant and μ_{g} is the mass of the molecular hydrogen.

In this work, by replacing Eq. (A.3) in Eq. (A.2) we estimated a value of α . We considered then that the snowline is located where the disk reaches a temperature of $T(r = r_{\text{ice}}) = T_{\text{ice}} = 140\text{K}$. Thus we could estimated the location of the snowline by

$$r_{\text{ice}} = R_{\star} \left(\frac{T_{\star}}{T_{\text{ice}}}\right)^2 \left(\frac{\alpha}{2}\right)^{\frac{1}{2}}. \quad (\text{A.4})$$

We estimated the location of the snowline at $r_{\text{ice}} = 0.42$ au, when the BD is 1 Myr-old, that is the initial time of our simulations. We considered this value fixed along all the simulations. As we know T_{\star} and R_{\star} evolve with time, the location of the snowline also would evolve getting closer to the star by time. If we consider that the location of the snowline is evolving with time, it could have important consequences regarding the final amount of water in mass of the resulting planets of the simulations. However, this treatment is out of the scope of this work.